processes

MDPI

Article

$NiS_{1-x}Se_x$ Nanoparticles Anchored on Nitrogen-Doped Reduced Graphene Oxide as Highly Stable Anode for Sodium-Ion Battery

Shunjiang Zhang, Ruirui Wang, Ronggen Cao *, Fang Fang and Renbing Wu

Department of Materials Science, Fudan University, Shanghai 200433, China; 20210300050@fudan.edu.cn (S.Z.); 19110300031@fudan.edu.cn (R.W.); f_fang@fudan.edu.cn (F.F.); rbwu@fudan.edu.cn (R.W.)
* Correspondence: caoronggen@fudan.edu.cn

Abstract: Nickel sulfides are regarded as one of the promising anode materials for sodium-ion batteries (SIBs), but the sluggish electrodes kinetics and rapid capacity decay, caused by their intrinsic low electrical conductivity and high bulk expansion, greatly limit their practical application. To overcome these obstacles, nano-sized, selenium-doped, nickel sulfide particles, anchored on nitrogen-doped reduced graphene oxide composites ($NiS_{1-x}Se_x$@N–rGO), are rationally synthesized. The broad Na^+ diffusion channels, resulting from Se doping, as well as the short Na^+ transferring path, attributed from nano-size scale of $NiS_{1-x}Se_x$ particles, endow $NiS_{1-x}Se_x$@N–rGO composites with ultrafast storage kinetics. Moreover, strong coupled effect between the $NiS_{1-x}Se_x$ and N–rGO is beneficial to the uniform dispersion of $NiS_{1-x}Se_x$ nanoparticles, improving electrical conductivity and suppressing the volume variation in charge/discharge process. Furthermore, the cut-off discharge voltage is modulated to realize the smaller volume change during cycle process. As a result, the fabricated anode of SIBs based on $NiS_{1-x}Se_x$@N–rGO composites exhibits a high specific capacity of 300 mAh g^{-1}, at the current density of 1 A g^{-1}, after 1000 cycles with almost no capacity degradation.

Keywords: sodium-ion batteries; Se doping; nickel sulfide; rGO nanosheet

Citation: Zhang, S.; Wang, R.; Cao, R.; Fang, F.; Wu, R. $NiS_{1-x}Se_x$ Nanoparticles Anchored on Nitrogen-Doped Reduced Graphene Oxide as Highly Stable Anode for Sodium-Ion Battery. *Processes* **2022**, *10*, 566. https://doi.org/10.3390/pr10030566

Academic Editor: Sara Pescetelli

Received: 10 February 2022
Accepted: 9 March 2022
Published: 14 March 2022

1. Introduction

Lithium-ion batteries (LIBs) have been extensively applied in all aspects of our lives, but the limited lithium resources cannot satisfy the ever-growing demand for future electrical storage system (EES) devices [1–6]. Sodium-ion batteries (SIBs) are deemed to be a highly promising alternative, due to the abundant resources, low-cost and, especially, similar working mechanism to LIBs [7–9]. However, graphite, as the conventional anode material of LIBs, is eliminated for SIBs, due to the larger atomic radius of sodium element [10–12]. Therefore, it is imperative to develop appropriate anode materials for SIBs. In the past years, a variety of anode materials, including hexagonal boron nitride (h–BN) [13], carbonaceous materials [14,15], alloy-based materials [16,17], transition metal oxides [18–20], and transition metal chalcogenides [21–23], have been explored as anode materials for SIBs. Among them, transition metal chalcogenides, especially nickel sulfides, have received much attention, due to their high specific capacity, rich resources, low-cost, and being environmentally benign [24–27]. However, the nickel sulfides suffer from a poor electrical conductivity and large volume expansion during charge/discharge process, leading to unsatisfactory specific capacity and fast capacity fading [9,28,29].

In order to address the above-mentioned issues, several effective strategies have been developed. The first one is optimizing nanostructure by reducing the size of materials to nanoscale, leading to a short ion-diffusion path and minimizing the effect of volume expansion [17,30]. The second one is introducing carbon matrix by compositing nickel-based sulfides with conductive carbon materials, such as graphene, carbon nanotube, and porous carbon, which demonstrated great promise in enhancing the electrical conductivity and

inhibiting the volume change [31,32]. The third one is tailoring chemical composition by doping with homologous nonmetallic elements, which not only boosts electrochemical activity but also significantly improves the physicochemical properties of various alkali ion transport [33–35]. For example, Yang et al. synthesized solid-solution $FeS_{2-x}Se_x$ microspheres as an anode material for SIBs. Benefiting from the increased layer spacing and improved electronic conductivity, the electrodes exhibited 275 mAh g^{-1} after 1000 cycles at 1 A g^{-1} [36]. Cao et al. reported Se-doped, nickel–cobalt sulfides for high-performance supercapacitor, demonstrating fast ion diffusion and low resistance characteristics after Se doping [37]. Furthermore, according to present studies, electrode materials suffer from irreversible loss of capacity and greater volume expansion under the fully discharged condition, so selecting a suitable cut-off discharge voltage would be beneficial to realize better cycling stability [12]. Despite the achievements that have been made, limited improvement of the sodium storage properties of nickel sulfides were achieved by each proposed strategy along, and the integration of all above-mentioned strategies remains a big challenge.

Herein, nano-sized, selenium-doped, nickel sulfide particles anchored on nitrogen-doped reduced graphene oxide ($NiS_{1-x}Se_x$@N–rGO) were successfully synthesized by hydrothermal reaction and subsequent sulfuration/selenization reaction. Benefiting from the nano-sized scale, broaden ion diffusion channels and strong coupling effect between $NiS_{1-x}Se_x$ nanoparticles and N–rGO, the NiS_{1-x}Sex@N–rGO composites possess enhanced electrochemical reaction kinetics and mitigated volume variation during cycling process. As expected, the obtained $NiS_{1-x}Se_x$@N–rGO composites, used as the anode material for SIBs, maintained a stable specific capacity of 300 mAh g^{-1}, after 1000 cycles 1 A g^{-1}, through regulating the cut-off discharge voltage.

2. Materials and Methods

2.1. Preparation of Spongy $Ni(OH)_2$@GO Precursor

Firstly, nickel nitrate hexahydrate (1 mmol) and 2–Methylimidazole (2–MeIm, 4 mmol) were dissolved in 5 mL CH_3OH, respectively, denoted as solutions A and B. Secondly, solutions A and B were successively added into 17 mL GO aqueous suspension (4 mg mL^{-1}), which was stirred for 10 min at room temperature to form suspension C. Then, suspension C was transferred into Teflon-lined autoclave and maintained at 180 °C for six hours. After cooled to room temperature, the black samples of $Ni(OH)_2$@GO was centrifuged and washed twice with CH_3OH and H_2O. Lastly, the obtained $Ni(OH)_2$@GO was blended with appropriate amounts of H_2O and freeze-dried at −50 °C for two days to obtain the spongy $Ni(OH)_2$@GO.

2.2. Preparation of $NiS_{1-x}Se_x$@N–rGO Composites

The spongy $Ni(OH)_2$@GO precursor and sulfur/selenium powder were placed at the head and last sides of a porcelain boat, then heated to 600 °C (2 °C min^{-1}), and they maintained this temperature for two hours in a flowing nitrogen atmosphere. Gaseous sulfur and selenium were driven by flowing nitrogen gas to react with the $Ni(OH)_2$@GO precursor to form the $NiS_{1-x}Se_x$@N–rGO composite. The preparation of NiS@N–rGO comparison samples was similar to $NiS_{1-x}Se_x$@N–rGO, except the absence of selenium powder.

2.3. Materials Characterizations

To observe the microstructure of the obtained samples, the field emission scanning electron microscope (FESEM, ZEIS, super–55) and transmission electron microscope (TEM, JEOL–2100) were employed. The phase composition was tested by X-ray diffractometer (XRD, D8 ADVANCE, Cu Kα–ray). The Raman spectra were measured on a Witec Alpha 300. The nitrogen adsorption–desorption isotherms measurement was performed on a JW–BK 100C instrument. The elemental states of samples were investigated using an X-ray energy spectrometer (Thermo Scientific, USA, ESCALAB 250XI). The weight loss curves of $NiS_{1-x}Se_x$@N–rGO and NiS@N–rGO composites were obtained by thermogravimetric analysis (MET–TLER TOLEDO TGA2).

2.4. Electrochemical Measurements

In order to fabricate working electrodes, the active material ($NiS_{1-x}Se_x$@N–rGO, 70 wt%), conductive carbon black (super–p, 20 wt%), and polyvinylidene fluoride (PVDF, 10 wt%) were dispersed in N-methyl pyrrolidone (NMP) solvent to make a slurry. The above prepared slurry was coated on the copper foil and then dried in vacuum at 70 °C for 12 h, which was subsequently cut into round films to be used as working electrodes. The half-cells were assembled in an argon-filled glove box (<0.5 ppm, H_2O and O_2). Na foil, Whatman glass fiber and 0.5 M $NaCF_3SO_3$ were utilized as counter electrode, separator, and electrolyte, respectively. The sodium storage performance at ambient temperature and effect of different voltage range (0.01–3.0 V and 0.3–3 V) for the assembled cells were obtained using the Land CT2001A battery testing system. AutoLab PGSTAT302N was employed to obtain the CV and EIS curves.

3. Results

The overall synthetic route for the synthesis of $NiS_{1-x}Se_x$@N–rGO composites is illustrated in Figure 1. First, the precursor of $Ni(OH)_2$, anchored on the surface of graphene oxide ($Ni(OH)_2$@GO), was fabricated by a simple hydrothermal reaction. It is noticed that 2-Methylimidazole (2-MeIm) was served as the nitrogen source and can facilitate the generation of sheet-like $Ni(OH)_2$ [38]. After a sulfuration/selenization reaction at high temperature (N_2 atmosphere), the $Ni(OH)_2$ was directly transformed into $NiS_{1-x}Se_x$ nanoparticles, and the GO was transformed into N–rGO simultaneously.

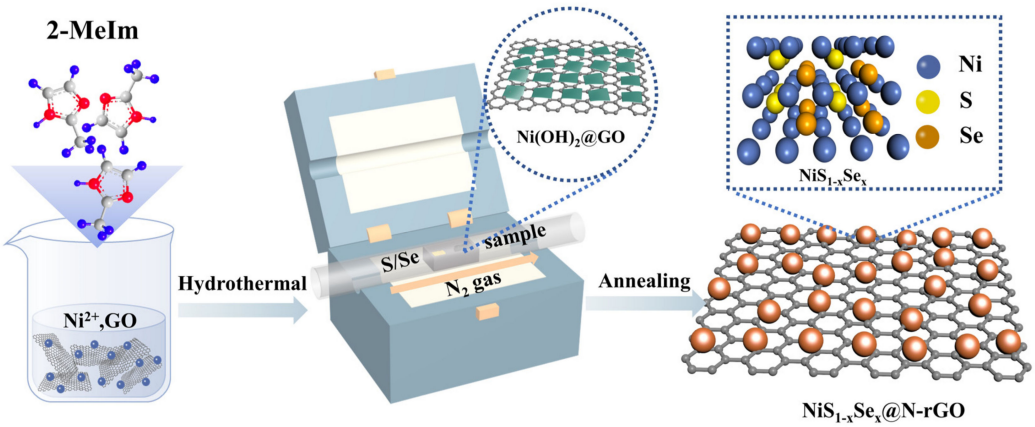

Figure 1. Schematic process of the formation of $NiS_{1-x}Se_x$@N–rGO composites.

The morphology and microstructure of the obtained samples were observed by FE-SEM and TEM. The FESEM images of $Ni(OH)_2$@GO precursors can be seen from Figure S1a,b. It is found that the sheet-like $Ni(OH)_2$ with smooth surface was compactly coated on the surface of GO, demonstrating a strong interaction force between them. After a sulfuration/selenization reaction, $Ni(OH)_2$@GO precursor was transformed into $NiS_{1-x}Se_x$ nanoparticles, uniformly anchored on N–rGO (Figure 2a,b). The NiS@N–rGO presented a similar structure with that of $NiS_{1-x}Se_x$@N–rGO composite (Figure S1c,d). The TEM images further demonstrated the homogeneous distribution of $NiS_{1-x}Se_x$ nanoparticles with diameters of 50–100 nm on N–rGO nanosheet (Figure 2c). In contrast, $NiS_{1-x}Se_x$ particles, converted from $Ni(OH)_2$, were gathered seriously (Figure S2), indicating that the addition of GO can serve to uniformly disperse the $NiS_{1-x}Se_x$ nanoparticles. Additionally, the lattice fringes with 0.281 nm can be clearly observed in Figure 2d, which corresponds to the (101) crystal plane of NiS. The fast Fourier transform (FFT) pattern (inset of Figure 2d) also confirmed the (101) crystal plane of NiS. However, the lattice spacing was slightly larger than that of standard NiS, indicating that Se elements with a larger radius were successfully doped into the lattice of NiS in $NiS_{1-x}Se_x$@N–rGO composites. Moreover, elemental mapping images revealed that Ni, Se, S, N, and C elements were well-distributed

in the $NiS_{1-x}Se_x$@N–rGO composites (Figure 2e–j), further confirming the well-doping of Se into NiS and successful synthesis of $NiS_{1-x}Se_x$@N–rGO composites.

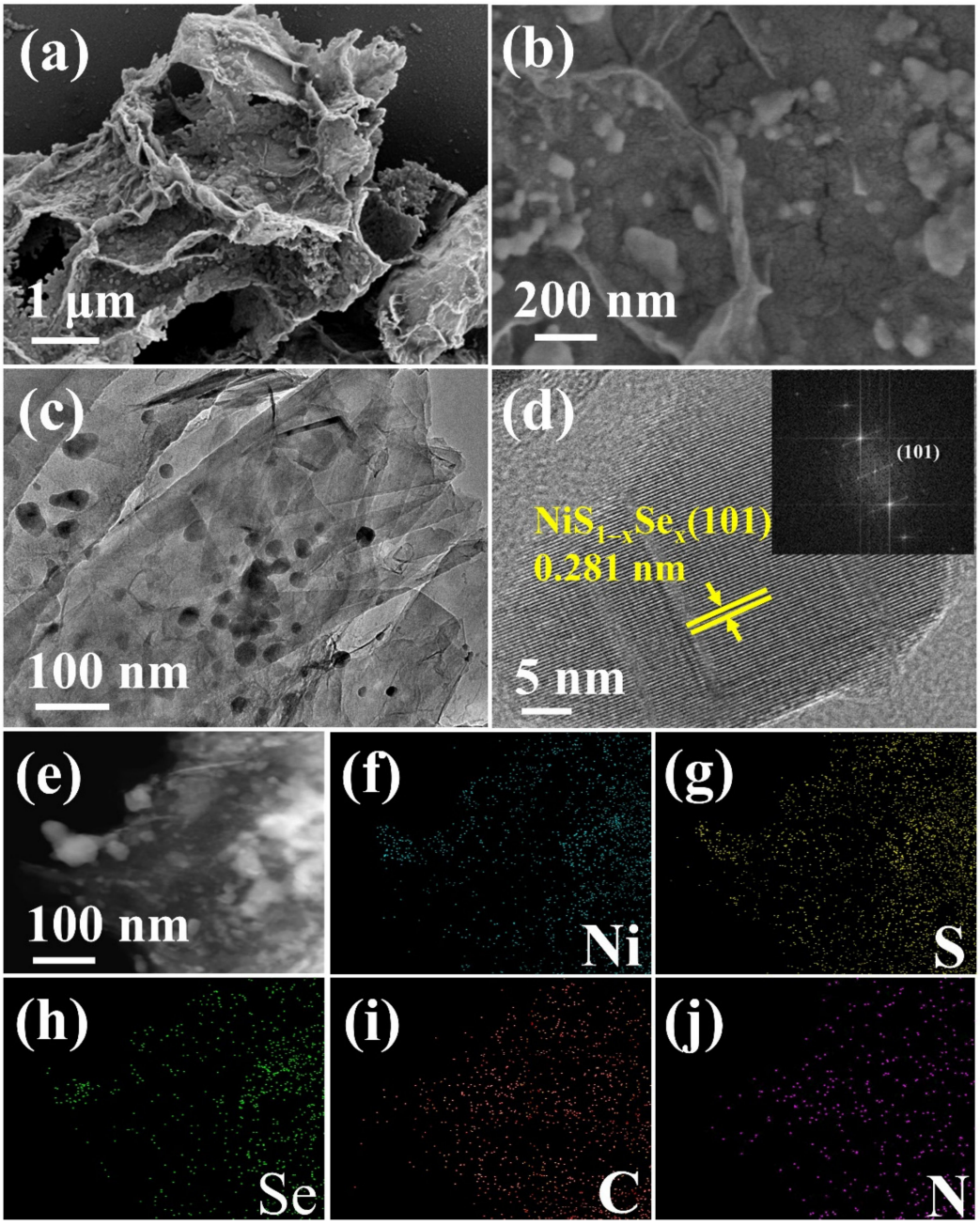

Figure 2. (**a**,**b**) FESEM, (**c**) TEM, (**d**) HRTEM and FFT pattern, and (**e**–**j**) elements mapping images of $NiS_{1-x}Se_x$@N–rGO composites.

In order to analyze the phase composition of the obtained samples, XRD characterization was implemented. Figure S3 was the diffraction peaks of the $Ni(OH)_2$@GO precursor, which was consistent with the crystallographic data of $Ni(OH)_2$ (JCPDS Card No. 14-0117). Five main peaks at 19.3°, 33.1°, 38.5°, 39.1°, and 52.1° can be attributed to the (001), (100), (101), (002), and (102) crystal planes of $Ni(OH)_2$. The NiS@N–rGO and $NiS_{1-x}Se_x$@N–rGO composites show similar crystal structure, corresponding to hexagonal NiS (JCPDS Card No. 02–1280). However, the diffraction peaks of the $NiS_{1-x}Se_x$@N–rGO composites shifted to a smaller angle, compared to the peaks of NiS, suggesting that the Se with a larger ionic radius (1.98 Å) was doped into NiS and enlarged the lattice spacing, without disturbing the crystal structure in the $NiS_{1-x}Se_x$@N–rGO composites. To further demonstrate the

successful doping of selenium, thermogravimetric analysis (TGA) characterization was conducted. As shown in Figure 3b, the TGA curves of the NiS@N–rGO and $NiS_{1-x}Se_x$@N–rGO composites exhibited similar weight loss trend, with the temperature increasing in O_2 atmosphere, except in the temperature range of 550–670 °C. In this temperature range, the NiS@N–rGO composites underwent a conversion reaction from nickel sulfide to nickel sulfate, followed by a partial decomposition reaction of nickel sulfate to nickel oxide, but the $NiS_{1-x}Se_x$@N–rGO composites were also accompanied by the breakdown of the Ni–Se bond [12,35,39].

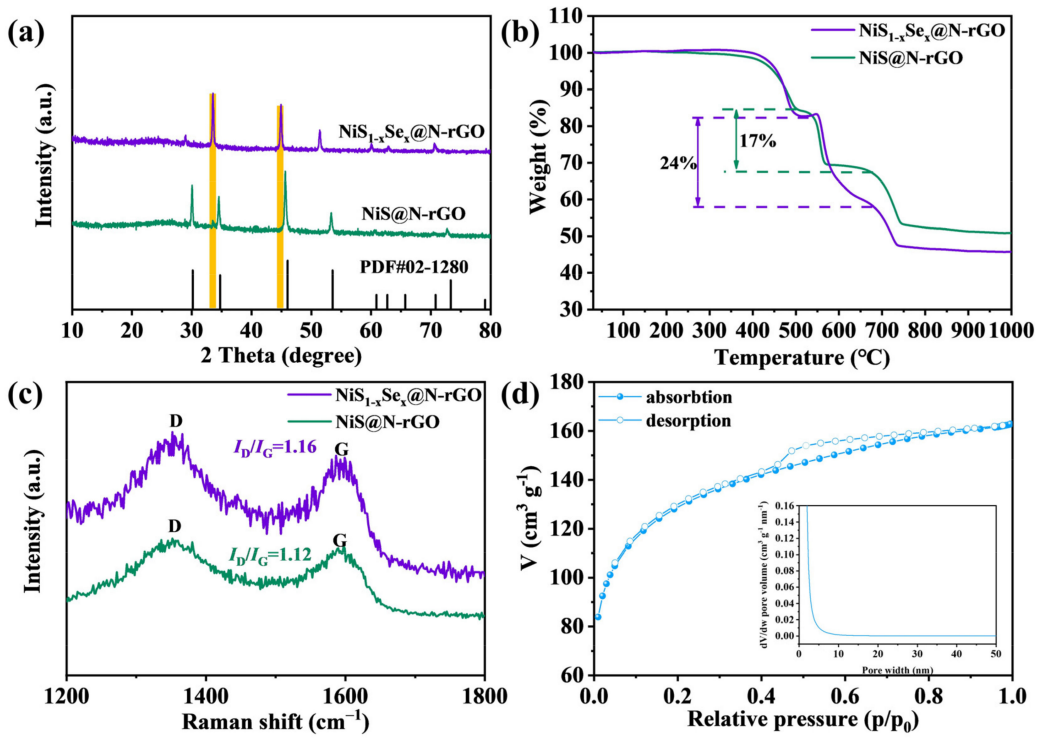

Figure 3. (**a**) XRD patterns, (**b**) TGA curves, (**c**) Raman spectra of NiS@N–rGO and $NiS_{1-x}Se_x$@N–rGO composites. (**d**) N_2 sorption isotherms and pore size distribution of $NiS_{1-x}Se_x$@N–rGO composites.

The Raman spectra of $NiS_{1-x}Se_x$@N–rGO and NiS@N–rGO are shown in Figure 3c. Two distinct peaks of graphite can be observed at ~1350 (D-band) and ~1580 cm^{-1} (G-band), which correspond to the disordered carbon and ordered graphitic carbon, respectively [40,41]. The peak intensity ratio (I_D/I_G) of $NiS_{1-x}Se_x$@N–rGO (1.16) is slightly higher than that of NiS@N–rGO (1.12), implying the abundance of defects and vacancies in $NiS_{1-x}Se_x$@N–rGO, which is favorable to improving the sodium storage kinetics [33,42]. The N_2 gas adsorption–desorption methodology was employed to investigate the porosity structure of $NiS_{1-x}Se_x$@N–rGO composites, and the result was presented in Figure 3d and Figure S4. The Brunauer–Emmett–Teller (BET) surface area of the $NiS_{1-x}Se_x$@N–rGO composites is as high as 431.7 $m^2\ g^{-1}$ (which is larger than 189.6 $m^2\ g^{-1}$ of NiS@N–rGO). Additionally, the pore size distribution of both is concentrated at ~2 nm (inset of Figure 3d and Figure S4b). Such a high BET surface area of $NiS_{1-x}Se_x$@N–rGO can be attributed to the three-dimensional structure of interconnected graphene and uniformly distribution of optimal pores. Importantly, this favorable structure can provide enough free space to accommodate the volume expansion of the $NiS_{1-x}Se_x$ nanoparticles during the cycle process and may greatly facilitate the penetration of the electrolyte.

To verify the chemical state and elemental composition of obtained samples, X-ray photoelectron spectroscopy (XPS) was performed. The surface chemical composition of the $NiS_{1-x}Se_x$@N–rGO composites can be accessed from Figure 4. It is evident that Ni, Se, S, C, and N elements all exist in $NiS_{1-x}Se_x$@N–rGO composites (Figure 4a). Notably, the peaks positions of C 1s (Figure 4b) and N 1s (Figure 4c) in NiS@N–rGO and $NiS_{1-x}Se_x$@N–rGO

composites are well in accordance with each other, suggesting the consistent chemical states of N–rGO in them. As seen in Figure 4b, three peaks located at 284.6, 285.6, and 286.3 eV were ascribed to the C–C, C–O, and C–N bonds, respectively [24,41]. As for the N 1s XPS spectrum in Figure 4c, three peaks at 399.0 eV, 400.8 eV, and 402.6 eV were assigned to pyridinic N, pyrrolic N, and graphitic N, respectively [43]. Importantly, due to the existing of the conjugation between the lone pair of electrons of the N atom and large π-bonds of the reduced graphene oxide lattice, the nitrogen doped in the reduced graphene oxide can enhance the electronic conductivity and provide more reactive sites [23,27,44–47].

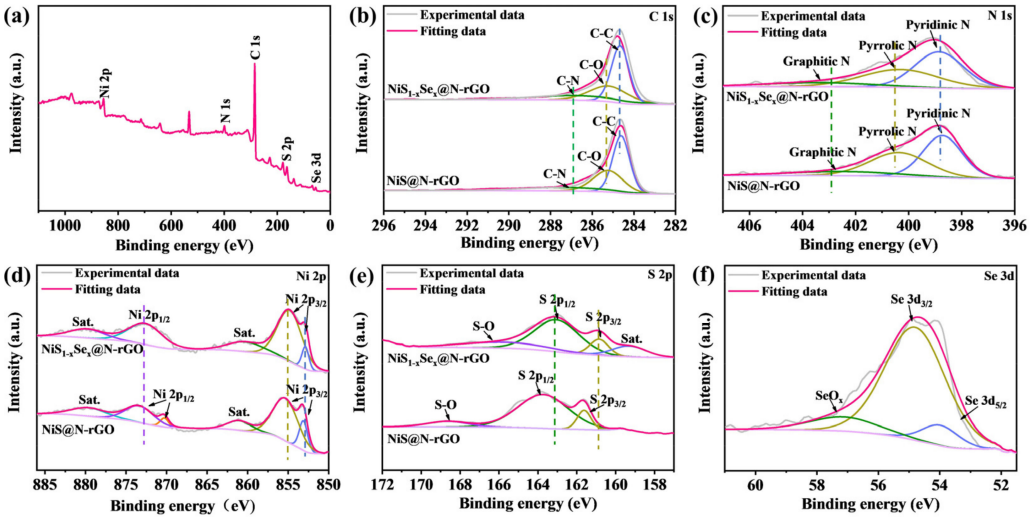

Figure 4. (**a**) XPS survey spectrum of $NiS_{1-x}Se_x$@N–rGO. (**b**–**e**) High-resolution C 1s, N 1s, Ni 2p, and S 2p contrast of NiS@N–rGO and $NiS_{1-x}Se_x$@N–rGO composites. (**f**) Se 3d XPS spectrum of $NiS_{1-x}Se_x$@N–rGO composites.

The high-resolution Ni 2p XPS spectra of $NiS_{1-x}Se_x$@N–rGO and NiS@N–rGO composites can be observed in Figure 4d. For $NiS_{1-x}Se_x$@N–rGO composite, the Ni 2p XPS spectrum showed five deconvoluted peaks. Two representative peaks at 852.9 and 855.0 eV were belong to Ni 2p3/2, while the peak at 872.8 eV were related to Ni 2p1/2 [48,49]. In addition to above three peaks, two accompanying satellite peaks at 860.5 and 879.8 eV were also observed. It was noticed that all the binding energy of Ni 2p3/2 and Ni 2p1/2 of $NiS_{1-x}Se_x$@N–rGO composites were slightly lower than those of NiS@N–rGO composites (Ni 2p3/2: 853.3 and 855.5 eV, Ni 2p1/2: 870.2 and 873.5 eV), implying that the homogeneous doping of Se with lower electronegativity reduces the binding energy of nickel ions. For the high-resolution S 2p spectrum of $NiS_{1-x}Se_x$@N–rGO (Figure 4e), the two major peaks located at 160.9 and 163.1 eV were attributed to S 2p3/2 and S 2p1/2, respectively, which are shifted to smaller binding energy, compared to those of peaks NiS@N–rGO (161.6 and 163.7 eV), suggesting the electronic structure of S element can be influenced by the Se element, with lower electronegativity. Additionally, two peaks at 159.3 and 165.8 eV in S 2p spectrum of $NiS_{1-x}Se_x$@N–rGO were ascribed to the accompanying satellite peak of S 2p and S–O band. The peaks change of Ni 2p and S 2p indicates that the uniformly doping of Se with lower electronegativity into the NiS can decrease the binding energy of NiS, which is highly beneficial to the conversion reaction [50]. The high-resolution Se 3d spectrum of $NiS_{1-x}Se_x$@N–rGO in Figure 4f can be divided into two well-fitted Se 3d5/2 and Se 3d3/2 peaks (located at 54.1 and 54.9 eV). The peak at 58.7 eV corresponds to the Se–O bond, reflecting the oxidation of the surface Se [49–51].

Inspired by the unique structural superiority, $NiS_{1-x}Se_x$@N–rGO composites was assessed as anode materials for SIBs, and the effect of cut-off discharge voltage for the electrochemical performance was investigated. The cyclic voltammetry (CV) curves were first collected with a scan rate of 0.1 mv s^{-1}, in two voltage ranges of 0.01–3 V and 0.3–3 V, respectively. In the first cathodic scan, in a voltage range of 0.01–3 V (Figure S5),

an obvious peak can be seen located at 1.02 V, corresponding to the sodium ion insertion of $NiS_{1-x}Se_x$@N–rGO ($NiS_{1-x}Se_x + \gamma Na^+ + \gamma e^- \leftrightarrow Na_\gamma NiS_{1-x}Se_x$, $Na_\gamma NiS_{1-x}Se_x + (2-\gamma)Na^+ + (2-\gamma)e^- \leftrightarrow Ni + (1-x)Na_2S + xNa_2Se$) and irreversible reaction associated with solid electrolyte interphase (SEI) formation [52–54]. In the first anodic scan, two broad peaks at 1.36 V, 1.79 V, and 2.25 V were associated with the oxidation reaction of Ni and the desodiation process [23,24,55,56]. The $NiS_{1-x}Se_x$@N–rGO composites, in the range of 0.3–3 V (Figure 5a), showed similar curves, compared to that at voltage range of 0.01–3 V, but the CV curves shape in subsequent cycles presented a stronger tendency to overlapping, suggesting a more stable reaction in the $NiS_{1-x}Se_x$@N–rGO electrode when the cut-off discharge voltage is 0.3 V [12]. In addition, Figure 5b provided the Coulombic efficiency for the first twenty charge/discharge cycles of $NiS_{1-x}Se_x$@N–rGO electrode at different cut-off discharge voltages at 0.2 A g^{-1}. It can be found that the Coulombic efficiency, under a cut-off discharge voltage of 0.3 V, is evidently higher in the first four cycles, while consistent in the following sixteen cycles, compared with that under the cut-off discharge voltage of 0.01 V, stating that a higher cut-off discharge voltage can avoid the occurrence of side reactions and, thus, increase the Coulombic efficiency.

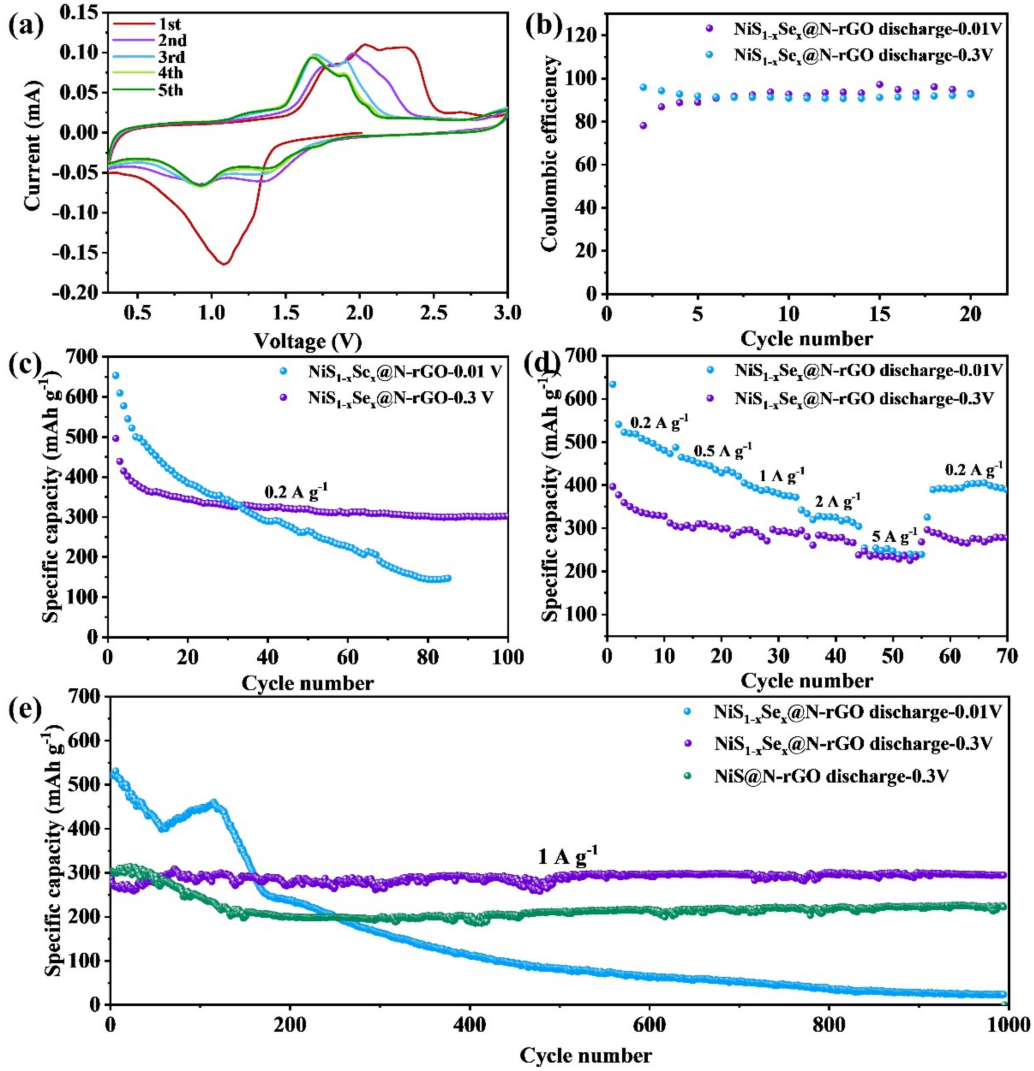

Figure 5. (**a**) CV curves at 0.3–3 V of $NiS_{1-x}Se_x$@N–rGO. (**b**) Coulombic efficiency at 0.2 A g^{-1}. (**c**,**d**) the cycling performance at 0.2 A g^{-1} and rate performance of the $NiS_{1-x}Se_x$@N–rGO electrode at different cut-off voltages. (**e**) The cycling performance of $NiS_{1-x}Se_x$@N–rGO and NiS@N–rGO electrode at 1 A g^{-1}.

Figure 5c shows the cycling performance of the $NiS_{1-x}Se_x$@N–rGO electrode at 0.2 A g^{-1}. It can be seen that the electrode maintained a high specific capacity of 305 mAh g^{-1} after 100 cycles when the cut-off discharge voltage is 0.3 V. However, as the cut-off discharge voltage is reduced to 0.01 V, the initial capacity is high (652 mAh g^{-1}), but the capacity rapidly decayed to 140 mAh g^{-1} after 80 cycles. The rate performance of the $NiS_{1-x}Se_x$@N–rGO electrode at different voltage range was also evaluated. As shown in Figure 5d, when employing a voltage range of 0.01–3 V, the average specific capacities were 507, 442, 391, 329, and 246 mAh g^{-1} at the current density of 0.2, 0.5, 1, 2, and 5 A g^{-1}, respectively. When the current density returned to 0.2 A g^{-1}, a normal specific capacity of 398 mAh g^{-1} was recovered, which is only 78.5% of the initial capacity. When employing the voltage range of 0.3–3 V, the ratio is 89.1%, indicating that the electrode material has superior reversibility in the voltage range of 0.3–3 V.

Figure 5e displays the cycling stability of $NiS_{1-x}Se_x$@N–rGO and NiS@N–rGO at 1 A g^{-1}. The $NiS_{1-x}Se_x$@N–rGO electrode could deliver a stable specific capacity of 300 mAh g^{-1} after 1000 cycles, with almost no capacity decay, when the electrodes were tested at the voltage range of 0.3–3 V. This cycling performance far surpasses that of NiS@N–rGO (200 mAh g^{-1} after 1000 cycles) and is also better than the previously reported transition metal-based sulfide and selenide anodes (Table S1). Meanwhile, the cycling performance of $NiS_{1-x}Se_x$@N–rGO at the voltage range of 0.01–3 V was also evaluated, which showed evident capacity fading and almost no capacity loss after 1000 cycles. The excellent cycling performance of $NiS_{1-x}Se_x$@N–rGO is ascribed to the structural advantage and optimal cut-off discharge voltage. First, the nanoscale of $NiS_{1-x}Se_x$ particles shorten the migration distance of Na^+, and Se-doping provides broad channels for Na^+ diffusion, which endows $NiS_{1-x}Se_x$@N–rGO with ultrafast storage kinetics. Second, N–rGO not only improves the electrical conductivity of the $NiS_{1-x}Se_x$ particle, but also suppresses their volume expansion during the charging and discharging process. Finally, the cut-off discharge voltage of the battery was optimized to achieve smaller volume expansion of $NiS_{1-x}Se_x$ during cycling process. In addition, to better understand the effect of Se doping for reaction kinetics of NiS, electrochemical impedance spectroscopy (EIS) tests were performed. As can be seen in Figure S6, $NiS_{1-x}Se_x$@N–rGO electrode has a smaller charge transfer resistance and Na^+ diffusion resistance, compared with that of NiS@N–rGO, revealing that the $NiS_{1-x}Se_x$@N–rGO electrodes possesses excellent electrical conductivity and feasible Na^+ ion diffusion ability.

4. Conclusions

In summary, we have developed an advanced anode material of SIBs, consisting of selenium-doped NiS nanoparticles, homogeneously anchored on nitrogen-doped reduced graphene oxide ($NiS_{1-x}Se_x$@N–rGO), through a facile hydrothermal and sulfuration/selenization process. In these delicate hybrid composites, the rGO can induce a synergistic coupling effect with nano-sized $NiS_{1-x}Se_x$, improving the electrical conductivity and alleviating the volume change. More importantly, Se doping into the NiS crystal structure led to broadened Na^+ channels and enhanced conversion reaction kinetics. Therefore, the $NiS_{1-x}Se_x$@N–rGO electrodes exhibit a highly stable specific capacity of 300 mAh g^{-1}, after 1000 cycles at 1 A g^{-1}, with almost no capacity degradation, by controlling the cut-off voltage (0.3–3.0 V).

Supplementary Materials: The following supporting information can be downloaded at: https://www.mdpi.com/article/10.3390/pr10030566/s1. Table S1: Electrochemical performance of the NiS1−xSex@N–rGO composite electrode, compared with the previously reported metal sulfide and metal selenide electrodes. Figure S1: (**a**,**b**) FESEM images of the $Ni(OH)_2$@GO precursor, and (**c**,**d**) FESEM images of NiS@N–rGO. Figure S2: FESEM images of (**a**,**b**) pure $Ni(OH)_2$ and (**c**,**d**) pure $NiS_{1-x}Se_x$. Figure S3: XRD pattern of Ni(OH)2@GO precursor. Figure S4: (**a**) N_2 sorption isotherms. (**b**) Pore size distribution of NiS@N–rGO composites. Figure S5: CV curves of NiS1−xSex@N–rGO electrode at 0.01–3 V. Figure S6: Electrochemical impedance spectra of $NiS_{1-x}Se_x$@N–rGO and NiS@N–rGO electrodes.

Author Contributions: Conceptualization, S.Z., R.W. (Ruirui Wang), and R.C.; methodology, R.C.; validation, R.W. (Ruirui Wang); investigation, F.F. and R.W. (Renbing Wu); resources, R.C.; data curation, S.Z.; writing—original draft preparation, S.Z.; writing—review and editing, R.W. (Ruirui Wang) and R.W. (Renbing Wu); supervision, R.C.; project administration, R.C.; funding acquisition, R.C. and R.W. (Renbing Wu). All authors have read and agreed to the published version of the manuscript.

Funding: This work was financially supported by the National Natural Science Foundation of China (Grant No. 52071087).

Data Availability Statement: Not applicable.

Conflicts of Interest: The authors declare no conflict of interest.

References

1. Ou, X.; Cao, L.; Liang, X.; Zheng, F.; Zheng, H.S.; Yang, X.; Wang, J.H.; Yang, C.; Liu, M. Fabrication of SnS_2/Mn_2SnS_4/carbon heterostructures for sodium–ion batteries with high initial coulombic efficiency and cycling stability. *ACS Nano* **2019**, *13*, 3666–3676. [CrossRef] [PubMed]
2. Wang, R.; Wu, R.; Yan, X.; Liu, D.; Guo, P.; Li, W.; Pan, H. Implanting single Zn atoms coupled with metallic Co nanoparticles into porous carbon nanosheets grafted with carbon nanotubes for high-performance lithium-sulfur batteries. *Adv. Funct. Mater.* **2022**, *32*, 2200424. [CrossRef]
3. Wu, R.; Qian, X.; Zhou, K.; Wei, J.; Lou, J.; Ajayan, P.M. Porous spinel $Zn_xCo_{3-x}O_4$ hollow polyhedra templated for high-rate lithium-ion batteries. *ACS Nano* **2014**, *8*, 6297–6303. [CrossRef] [PubMed]
4. Wang, R.; Wu, R.; Ding, C.; Chen, Z.; Xu, H.; Liu, Y.; Zhang, J.; Ha, Y.; Fei, B.; Pan, H. Porous carbon architecture assembled by cross-linked carbon leaves with implanted atomic cobalt for high-performance Li-S batteries. *Nano-Micro Lett.* **2021**, *13*, 151. [CrossRef]
5. Fan, S.; Huang, S.; Chen, Y.; Shang, Y.; Wang, Y.; Kong, D.; Pam, M.E.; Shi, L.; Lim, Y.W.; Shi, Y.; et al. Construction of complex NiS multi-shelled hollow structures with enhanced sodium storage. *Energy Storage Mater.* **2019**, *23*, 17–24. [CrossRef]
6. Liu, Y.; Chen, Z.; Jia, H.; Xu, H.; Liu, M.; Wu, R. Iron-doping-induced phase transformation in dual-carbon-confined cobalt diselenide enabling superior lithium storage. *ACS Nano* **2019**, *13*, 6113–6124. [CrossRef]
7. Ali, Z.; Zhang, T.; Asif, M.; Zhao, L.; Yu, Y.; Hou, Y. Transition metal chalcogenide anodes for sodium storage. *Mater. Today* **2020**, *35*, 131–167. [CrossRef]
8. Huang, Y.; Wang, Z.; Guan, M.; Wu, F.; Chen, R. Toward rapid-charging sodium–ion batteries using hybrid-phase molybdenum sulfide selenide-based anodes. *Adv. Mater.* **2020**, *32*, 2003534. [CrossRef]
9. General synthesis of dual carbon-confined metal sulfides quantum dots toward high-performance anodes for sodium-ion batteries. *Adv. Funct. Mater.* **2017**, *27*, 1702046. [CrossRef]
10. Dai, H.; Tang, M.; Huang, J.; Wang, Z. A series of molecule-intercalated MoS_2 as anode materials for sodium ion batteries. *ACS Appl. Mater. Interfaces* **2021**, *13*, 10870–10877. [CrossRef]
11. Liu, Y.; Qiao, Y.; Wei, G.; Li, S.; Lu, Z.; Wang, X.; Lou, X. Sodium storage mechanism of N, S co-doped nanoporous carbon: Experimental design and theoretical evaluation. *Energy Storage Mater.* **2018**, *11*, 274–281. [CrossRef]
12. Ou, X.; Li, J.; Zheng, F.; Wu, P.; Pan, Q.; Xiong, X.; Yang, C.; Liu, M. In situ X-ray diffraction characterization of $NiSe_2$ as a promising anode material for sodium ion batteries. *J. Power Sources* **2017**, *343*, 483–491. [CrossRef]
13. Angizi, S.; Alem, S.A.A.; Pakdel, A. Towards integration of two-dimensional hexagonal boron nitride (2D h–BN) in energy conversion and storage devices. *Energies* **2022**, *15*, 1162. [CrossRef]
14. Fan, L.; Lu, B. Reactive oxygen-doped 3D interdigital carbonaceous materials for Li and Na ion batteries. *Small* **2016**, *12*, 2783–2791. [CrossRef]
15. Kong, L.; Zhu, J.; Shuang, W.; Bu, X.-H. Nitrogen-doped wrinkled carbon foils derived from MOF nanosheets for superior sodium storage. *Adv. Energy Mater.* **2018**, *8*, 1801515. [CrossRef]
16. Kim, C.; Lee, K.-Y.; Kim, I.; Park, J.; Cho, G.; Kim, K.-W.; Ahn, J.-H.; Ahn, H.-J. Long-term cycling stability of porous Sn anode for sodium–ion batteries. *J. Power Sources* **2016**, *317*, 153–158. [CrossRef]

17. Zhang, N.; Liu, Y.; Lu, Y.; Han, X.; Cheng, F.; Chen, J. Spherical nano–Sb@C composite as a high-rate and ultra-stable anode material for sodium–ion batteries. *Nano Res.* **2015**, *8*, 3384–3393. [CrossRef]
18. Li, C.; Chen, T.; Xu, W.; Lou, X.; Pan, L.; Chen, Q.; Hu, B. Mesoporous nanostructured Co_3O_4 derived from MOF template: A high-performance anode material for lithium–ion batteries. *J. Mater. Chem. A* **2015**, *3*, 5585–5591. [CrossRef]
19. Zhang, L.; He, W.; Ling, M.; Shen, K.; Liu, Y.; Guo, S. Self-standing $MgMoO_4$/reduced graphene oxide nanosheet arrays for lithium and sodium ion storage. *Electrochim. Acta* **2017**, *252*, 322–330. [CrossRef]
20. Zhao, C.; Yu, C.; Zhang, M.; Huang, H.; Li, S.; Han, X.; Liu, Z.; Yang, J.; Xiao, W.; Liang, J.; et al. Ultrafine MoO_2–carbon microstructures enable ultralong-life power-type sodium ion storage by enhanced pseudocapacitance. *Adv. Energy Mater.* **2017**, *7*, 1602880. [CrossRef]
21. Hu, Z.; Zhu, Z.; Cheng, F.; Zhang, K.; Wang, J.; Chen, C.; Chen, J. Pyrite FeS_2 for high-rate and long-life rechargeable sodium batteries. *Energy Env. Sci.* **2015**, *8*, 1309–1316. [CrossRef]
22. Li, D.; Sun, Y.; Chen, S.; Yao, J.; Zhang, Y.; Xia, Y.; Yang, D. Highly porous FeS/carbon fibers derived from Fe-carrageenan biomass: High-capacity and durable anodes for sodium–ion batteries. *ACS Appl. Mater. Interfaces* **2018**, *10*, 17175–17182. [CrossRef]
23. Dong, C.; Liang, J.; He, Y.; Li, C.; Chen, X.; Guo, L.; Tian, F.; Qian, Y.; Xu, L. $NiS_{1.03}$ hollow spheres and cages as superhigh rate capacity and stable anode materials for half/full sodium–ion batteries. *ACS Nano* **2018**, *12*, 8277–8287. [CrossRef]
24. Zhao, F.; Gong, Q.; Traynor, B.; Zhang, D.; Li, J.; Ye, H.; Chen, F.; Han, N.; Wang, Y.; Sun, X.; et al. Stabilizing nickel sulfide nanoparticles with an ultrathin carbon layer for improved cycling performance in sodium ion batteries. *Nano Res.* **2016**, *9*, 3162–3170. [CrossRef]
25. Mahmood, N.; Zhang, C.; Hou, Y. Nickel sulfide/nitrogen-doped graphene composites: Phase-controlled synthesis and highperformance anode materials for lithium ion batteries. *Small* **2013**, *9*, 1321–1328. [CrossRef]
26. Tao, H.; Zhou, M.; Wang, K.; Cheng, S.; Jiang, K. Nickel sulfide nanospheres anchored on reduced graphene oxide in situ doped with sulfur as a high performance anode for sodium–ion batteries. *J. Mater. Chem. A* **2017**, *5*, 9322–9328. [CrossRef]
27. Shuang, W.; Huang, H.; Kong, L.; Zhong, M.; Li, A.; Wang, D.; Xu, Y.; Bu, X.-H. Nitrogen-doped carbon shell-confined Ni_3S_2 composite nanosheets derived from Ni–MOF for high performance sodium–ion battery anodes. *Nano Energy* **2019**, *62*, 154–163. [CrossRef]
28. Pan, Q.; Tong, Z.; Su, Y.; Qin, S.; Tang, Y. Energy storage mechanism, challenge and design strategies of metal sulfides for rechargeable sodium/potassium-ion batteries. *Adv. Funct. Mater.* **2021**, *31*, 2103912. [CrossRef]
29. Chen, J.; Li, S.; Kumar, V.; Lee, P.S. Carbon coated bimetallic sulfide hollow nanocubes as advanced sodium ion battery anode. *Adv. Energy Mater.* **2017**, *7*, 1700180. [CrossRef]
30. Shangguan, H.; Huang, W.; Engelbrekt, C.; Zheng, X.; Shen, F.; Xiao, X.; Ci, L.; Si, P.; Zhang, J. Well-defined cobalt sulfide nanoparticles locked in 3D hollow nitrogen-doped carbon shells for superior lithium and sodium storage. *Energy Storage Mater.* **2019**, *18*, 114–124. [CrossRef]
31. Sun, W.; Zhao, W.; Yuan, S.; Zhang, L.; Yang, Y.; Ge, P.; Ji, X. Designing rational interfacial bonds for hierarchical mineral-type trogtalite with double carbon towards ultra-fast sodium-ions storage properties. *Adv. Funct. Mater.* **2021**, *31*, 2100156. [CrossRef]
32. Zhang, X.; Weng, W.; Gu, H.; Hong, Z.; Xiao, W.; Wang, F.R.; Li, W.; Gu, D. Versatile preparation of mesoporous single-layered transition–metal sulfide/carbon composites for enhanced sodium storage. *Adv. Mater.* **2022**, *34*, 2104427. [CrossRef] [PubMed]
33. Wang, C.; Zhang, B.; Xia, H.; Cao, L.; Luo, B.; Fan, X.; Zhang, J.; Ou, X. Composition and architecture design of double-shelled $Co_{0.85}Se_{1-x}S_x$@carbon/graphene hollow polyhedron with superior alkali (Li, Na, K)–ion storage. *Small* **2020**, *16*, 1905853. [CrossRef] [PubMed]
34. Jia, G.; Chao, D.; Tiep, N.H.; Zhang, Z.; Fan, H.J. Intercalation Na–ion storage in two-dimensional $MoS_{2-x}Se_x$ and capacity enhancement by selenium substitution. *Energy Storage Mater.* **2018**, *14*, 136–142. [CrossRef]
35. Cao, D.; Wang, Y.; Kang, W.; Li, C.; Cao, D.; Fan, L.; Wang, R.; Sun, D. ZnS_xSe_{1-x}/N–C (x = 0.24) hierarchical nanosphere with improved energy storage capability as sodium–ion battery anode. *J. Alloy. Compd.* **2019**, *771*, 147–155. [CrossRef]
36. Long, Y.; Yang, J.; Gao, X.; Xu, X.; Fan, W.; Yang, J.; Hou, S.; Qian, Y. Solid-solution anion-enhanced electrochemical performances of metal sulfides/selenides for sodium–ion capacitors: The case of $FeS_{2-x}Se_x$. *ACS Appl. Mater. Interfaces* **2018**, *10*, 10945–10954. [CrossRef]
37. Lin, J.; Zhong, Z.; Wang, H.; Zheng, X.; Wang, Y.; Qi, J.; Cao, J.; Fei, W.; Huang, Y.; Feng, J. Rational constructing free-standing Se doped nickel–cobalt sulfides nanotubes as battery-type electrode for high-performance supercapattery. *J. Power Sources* **2018**, *407*, 6–13. [CrossRef]
38. Qiu, C.; Cai, F.; Wang, Y.; Liu, Y.; Wang, Q.; Zhao, C. 2–Methylimidazole directed ambient synthesis of zinc–cobalt LDH nanosheets for efficient oxygen evolution reaction. *J. Colloid Interface Sci.* **2020**, *565*, 351–359. [CrossRef]
39. Zhao, G.; Zhang, Y.; Yang, L.; Jiang, Y.; Zhang, Y.; Hong, W.; Tian, Y.; Zhao, H.; Hu, J.; Zhou, L.; et al. Nickel chelate derived NiS_2 decorated with bifunctional carbon: An efficient strategy to promote sodium storage performance. *Adv. Funct. Mater.* **2018**, *28*, 1803690. [CrossRef]
40. Li, B.; Wang, R.; Chen, Z.; Sun, D.; Fang, F.; Wu, R. Embedding heterostructured MnS/Co1-xS nanoparticles in porous carbon/graphene for superior lithium storage. *J. Mater. Chem. A* **2019**, *7*, 1260–1266. [CrossRef]
41. Zhao, X.; Wang, H.-E.; Massé, R.C.; Cao, J.; Sui, J.; Li, J.; Cai, W.; Cao, G. Design of coherent anode materials with 0D Ni_3S_2 nanoparticles self-assembled on 3D interconnected carbon networks for fast and reversible sodium storage. *J. Mater. Chem. A* **2017**, *5*, 7394–7402. [CrossRef]

42. Wang, R.; Li, B.; Lai, L.; Hou, M.; Gao, J.; Wu, R. 3D urchin-like architectures assembled by MnS nanorods encapsulated in N-doped carbon tubes for superior lithium storage capability. *Chem. Eng. J.* **2019**, *355*, 752–759. [CrossRef]
43. Xu, S.; Li, Z.; Chu, K.; Yao, G.; Xu, Y.; Niu, P.; Yang, Y.; Chen, Q.; Zheng, F. Construction of NiS nanosheets anchored on the inner surface of nitrogen-doped hollow carbon matrixes with enhanced sodium and potassium storage performances. *Acs Appl. Energy Mater.* **2021**, *4*, 662–670. [CrossRef]
44. Zhao, L.; He, R.; Rim, K.T.; Schiros, T.; Kim, K.S.; Zhou, H.; Gutierrez, C.; Chockalingam, S.P.; Arguello, C.J.; Palova, L.; et al. Visualizing individual nitrogen dopants in monolayer graphene. *Science* **2011**, *333*, 999–1003. [CrossRef]
45. Qutaish, H.; Lee, J.; Hyeon, Y.; Han, S.A.; Lee, I.-H.; Heo, Y.-U.; Whang, D.; Moon, J.; Park, M.-S.; Kim, J.H. Design of cobalt catalysed carbon nanotubes in bimetallic zeolitic imidazolate frameworks. *Appl. Surf. Sci.* **2021**, *547*, 149134. [CrossRef]
46. Hyeon, Y.; Lee, J.; Qutaish, H.; Han, S.A.; Choi, S.H.; Moon, S.W.; Park, M.-S.; Whang, D.; Kim, J.H. Lithium metal storage in zeolitic imidazolate framework derived nanoarchitectures. *Energy Storage Mater.* **2020**, *33*, 95–107. [CrossRef]
47. Lee, J.; Choi, S.H.; Qutaish, H.; Hyeon, Y.; Han, S.A.; Heo, Y.-U.; Whang, D.; Lee, J.-W.; Moon, J.; Park, M.-S.; et al. Structurally stabilized lithium–metal anode via surface chemistry engineering. *Energy Storage Mater.* **2021**, *37*, 315–324. [CrossRef]
48. Yi, M.; Wu, A.; Chen, Q.; Cai, D.; Zhan, H. In situ confined conductive nickel cobalt sulfoselenide with tailored composition in graphitic carbon hollow structure for energy storage. *Chem. Eng. J.* **2018**, *351*, 678–687. [CrossRef]
49. Chen, N.; Du, Y.-X.; Zhang, G.; Lu, W.-T.; Cao, F.-F. Amorphous nickel sulfoselenide for efficient electrochemical urea-assisted hydrogen production in alkaline media. *Nano Energy* **2021**, *81*, 105605. [CrossRef]
50. Tian, Y.; Zhang, Y.; Huang, A.; Wen, M.; Wu, Q.; Zhao, L.; Wang, M.; Shen, Y.; Wang, Z.; Fu, Y. Nanostructured Ni_2SeS on porous–carbon skeletons as highly efficient electrocatalyst for hydrogen evolution in acidic medium. *Inorg. Chem.* **2020**, *59*, 6018–6025. [CrossRef]
51. Park, G.D.; Park, J.-S.; Kim, J.K.; Kang, Y.C. Metal sulfoselenide solid solution embedded in porous hollow carbon nanospheres as effective anode material for potassium–ion batteries with long cycle life and enhanced rate performance. *Chem. Eng. J.* **2022**, *428*, 131051. [CrossRef]
52. Li, J.; Li, J.; Yan, D.; Hou, S.; Xu, X.; Lu, T.; Yao, Y.; Mai, W.; Pan, L. Design of pomegranate-like clusters with NiS_2 nanoparticles anchored on nitrogen-doped porous carbon for improved sodium ion storage performance. *J. Mater. Chem. A* **2018**, *6*, 6595–6605. [CrossRef]
53. Zhao, X.; Gong, F.; Zhao, Y.; Huang, B.; Qian, D.; Wang, H.-E.; Zhang, W.; Yang, Z. Encapsulating NiS nanocrystal into nitrogen-doped carbon framework for high performance sodium/potassium–ion storage. *Chem. Eng. J.* **2020**, *392*, 123675. [CrossRef]
54. Zhang, Z.; Shi, X.; Yang, X. Synthesis of core–shell NiSe/C nanospheres as anodes for lithium and sodium storage. *Electrochim. Acta* **2016**, *208*, 238–243. [CrossRef]
55. Su, C.; Ru, Q.; Cheng, S.; Gao, Y.; Chen, F.; Zhao, L.; Ling, F.C.-C. 3D pollen-scaffolded NiSe composite encapsulated by MOF-derived carbon shell as a high–low temperature anode for Na–ion storage. *Compos. Part B Eng.* **2019**, *179*, 107538. [CrossRef]
56. Zhu, K.J.; Liu, G.; Wang, Y.J.; Liu, J.; Li, S.T.; Yang, L.Y.; Liu, S.L.; Wang, H.; Xie, T. Metal–organic frameworks derived novel hierarchical durian-like nickel sulfide (NiS_2) as an anode material for high-performance sodium–ion batteries. *Mater. Lett.* **2017**, *197*, 180–183. [CrossRef]